Spatial Distribution of the Pedersen Conductance in the Jovian Aurora From Juno-UVS Spectral Images

J. -C. Gérard, L. Gkouvelis, B. Bonfond, D. Grodent, G. R. Gladstone, V. Hue, T. K. Greathouse, M. Versteeg, J. A. Kammer, M. Blanc

JGR Space Physics

RESEARCH ARTICLE
10.1029/2020JA028142

Special Section:
Jupiter Midway Through the Juno Mission

Spatial Distribution of the Pedersen Conductance in the Jovian Aurora From Juno-UVS Spectral Images

J.-C. Gérard[1], L. Gkouvelis[1], B. Bonfond[1], D. Grodent[1], G. R. Gladstone[2], V. Hue[2], T. K. Greathouse[2], M. Versteeg[2], J. A. Kammer[2], and M. Blanc[3]

[1]LPAP, STAR Institute, Université de Liège, Liège, Belgium, [2]Southwest Research Institute, San Antonio, TX, USA, [3]IRAP, Observatoire Midi-Pyrennées, Toulouse, France

Key Points:
- Multispectral auroral observations from UVS-Juno are used to map the auroral ionospheric Pedersen conductance in both hemispheres
- H_3^+ and hydrocarbon ions make most of the contribution to auroral ionospheric conductance
- The conductance varies from less than 0.1 up to several mhos in the main aurora, high latitude precipitation, and Io magnetic footprint

Supporting Information:
- Supporting Information S1
- Figure S1
- Figure S2
- Figure S3
- Figure S4
- Figure S5
- Figure S6
- Figure S7
- Figure S8

Correspondence to:
J.-C. Gérard,
jc.gerard@uliege.be

Citation:
Gérard, J.-C., Gkouvelis, L., Bonfond, B., Grodent, D., Gladstone, G. R., Hue, V., et al. (2020). Spatial distribution of the Pedersen conductance in the Jovian aurora from Juno-UVS spectral images. *Journal of Geophysical Research: Space Physics*, *125*, e2020JA028142. https://doi.org/10.1029/2020JA028142

Received 22 APR 2020
Accepted 1 JUL 2020
Accepted article online 16 JUL 2020

Abstract Ionospheric conductivity perpendicular to the magnetic field plays a crucial role in the electrical coupling between planetary magnetospheres and ionospheres. At Jupiter, it controls the flow of ionospheric current from above and the closure of the magnetosphere-ionosphere circuit in the ionosphere. We use multispectral images collected with the Ultraviolet Spectral (UVS) imager on board Juno to estimate the two-dimensional distribution of the electron energy flux and characteristic energy. These values are fed to an ionospheric model describing the generation and loss of different ion species, to calculate the auroral Pedersen conductivity. The vertical distributions of H_3^+, hydrocarbon ions, and electrons are calculated at steady state for each UVS pixel to characterize the spatial distribution of electrical conductance in the auroral region. We find that the main contribution to the Pedersen conductance stems from collisions of $H_3^+$and heavier ions with H_2. However, hydrocarbon ions contribute as much as 50% to Σ_p when the auroral electrons penetrate below the homopause. The largest values are usually associated with the bright main emission, the Io auroral footprint and occasional bright emissions at high latitude. We present examples of maps for both hemispheres based on Juno-UVS images, with Pedersen conductance ranging from less than 0.1 to a few mhos.

Plain Language Summary One of the quantities characterizing the ability of ionospheres to carry currents perpendicular to the magnetic field is the altitude integrated Pedersen conductivity. On Jupiter, it is an important quantity that partly controls how electric currents can flow between the magnetosphere and the high-latitude ionosphere. It is therefore a key element in the understanding of how and where the Jovian aurora is formed and an important input to numerical models of auroral precipitation. We use observations from the UltraViolet spectral imager near Juno's closest approach to Jupiter to remotely characterize the flux of energy carried by the auroral electrons and their mean energy. These quantities are evaluated for each instrumental pixel and used as inputs to a model to map the Pedersen integrated conductivity. The main contributions to the conductance are caused by collisions between H_3^+ and hydrocarbon ions such as CH_5^+ and $C_3H_n^+$ with neutral constituents. We present examples of Pedersen conductance maps for both hemispheres. We find that the conductance is spatially very variable with values ranging from less than 0.1 to several mhos. The largest values are usually associated with the bright main emission, the Io auroral footprint and occasional bright emissions at high latitude.

1. Introduction

The ionospheric Pedersen (Σ_p) and Hall conductances (Σ_h), which are the altitude-integrated values of the corresponding local conductivities, play a crucial role in the electrical coupling between planetary magnetospheres and ionospheres. They are considerably enhanced at high latitudes by ionization resulting from the interaction of auroral electron precipitation with upper atmospheres. Their magnitude and spatial distribution are therefore important elements to take into account in models of magnetosphere-ionosphere-thermosphere coupling. At Jupiter, the current system flowing between the magnetosphere and the ionosphere depends on the availability of electric charges along the high-latitude magnetic field line and the limiting values of ionospheric conductances. According to the current loop system conceptual model (Cowley & Bunce, 2001; Ray et al., 2015; Tao et al., 2009), the auroral Pedersen conductance Σ_p allows the closure of magnetic-field-aligned electric currents (referred to as FACs) into and out of the ionosphere. The Pedersen current flows in the direction perpendicular to the magnetic field lines and parallel to the electric field direction. It is in turn modulated by the auroral precipitation that enhances ionization and

increases the density of electric charges available to carry it across field lines. Although the observed distribution of FACs appears more complex and fragmented than in these early magnetosphere-ionosphere (M-I) models (Kotsiaros et al., 2019), the ionospheric Pedersen conductance plays an important role in the transfer of momentum and energy between the magnetosphere and the ionosphere of Jupiter. In particular, whatever the importance of Hall currents, it is the value of the Pedersen conductance that determines the amount of Joule power dissipation of the M-I circuit into the ionosphere/thermosphere.

Values of the Pedersen conductance in the literature have been discussed in reviews by Clarke et al. (2004) and Badman et al. (2015). Strobel and Atreya (1983) estimated the Jovian Pedersen conductance to be on the order of 10 mhos in the case of a bright aurora as had been observed by Voyager for a B = 8 nT. Singhal (1996) found that an important contribution originates from heavy hydrocarbon ions. Based on theoretical estimates of the electron density profiles, he estimated the auroral conductance to be 1.8 mho for a magnetic field intensity of 10 nT. Millward et al. (2002) found Σ_p values up to 1.7 mho for a 10 mW m^{-2} precipitation of initial energy E_0 of 60 keV electrons. Nichols and Cowley (2004) introduced the concept of a feedback between the auroral electron precipitation and the Pedersen conductance. They showed that the modification of the Pedersen conductance by auroral precipitation has an impact on the distribution and intensity of the FACs closure into the auroral ionosphere. Their Pedersen conductivity value was based on Millward et al.'s (2002) model adapted to account for the value of the precipitated electron energy flux. In their M-I coupling model, the enhanced value of Σ_p increases the efficiency of the transfer of the planet's angular momentum to the plasma of the magnetosphere. Based on a 1-D model, Hiraki and Tao (2008) estimated the Pedersen conductivity ~0.5 mho for a precipitated energy flux of 22 mW m^{-2} with E_0 = 100 keV, while Tao et al. (2009) showed a latitudinal cut of Σ_p peaking at 0.75 mho. Using the 3-D JIM model (Achilleos et al., 1998), Smith and Aylward (2009) employed a conductivity model derived from a model of the auroral ionosphere where the shape of the vertical profile of conductivity at each given pressure level was the same at all latitudes, even if the absolute conductivities depended on latitude. They estimated Σ_p between 1.3 and 1.5 mho. The JTGCM M-I model by Bougher et al. (2005) and Majeed et al. (2009) predicted large conductances of about 12 mhos in the Northern Hemisphere. Ray et al. (2012) obtained a latitudinal peak of 0.75 mho for their baseline model corresponding to F_e = 10 mW m^{-2} and E_0 = 60 keV. The large range and diversity of conductance values between these studies is mostly explained by the different assumptions about the electron fluxes and mean energy of the precipitating electrons. These uncertainties largely result from of the lack of observational constraints in the auroral regions. Another source of differences is the fate of the electric charge carried by H_3^+ ions after they react with methane near and below the homopause. Most of the earlier studies did not include consideration of the hydrocarbon ions in the multilayered ionosphere.

The value of spectral remote sensing from space to derive conductances in the Earth's polar ionosphere has been demonstrated using Far Ultraviolet (FUV) multispectral images collected by polar orbiting satellites (Coumans et al., 2004; Germany et al., 1994). Comparisons of measurements of the auroral electron flux on board Juno with the auroral brightness indicates that using in situ measurements to determine the characteristics of the electron beam reaching the Jovian atmosphere is difficult, especially in the high-latitude regions (Gérard et al., 2019). Therefore, we use multispectral images collected with the UltraViolet Spectral (UVS) instrument on board the Juno spacecraft orbiting Jupiter (Bagenal et al., 2017; Bolton et al., 2017) to characterize the spatial distribution of electrical conductance in the auroral region.

2. Methodology

Our method is based on the use of Juno-UVS multispectral images of auroral and polar emissions. Juno-UVS (Gladstone et al., 2017) is an ultraviolet imaging spectrograph operating in the 68 to 210 nm range including the H_2 Werner and Lyman bands emissions. The “dog bone” entrance slit is made of three segments with fields of view of 0.2° × 2.5°, 0.025° × 2.0°, and 0.2° × 2.5°. Global images of both polar regions are reconstructed by taking advantage of the spacecraft rotation, as the field of view sweeps across the planet at each rotation. Using a neutral atmosphere model and an electron transport code, it is possible to retrieve characteristics of the precipitating electron populations from the observation of the photons they produce.

The precipitated energy flux reaching the atmosphere is obtained from the integration of the unabsorbed H_2 auroral brightness observed with UVS between 155 and 162 nm (Bonfond et al., 2017) in every UVS pixel.

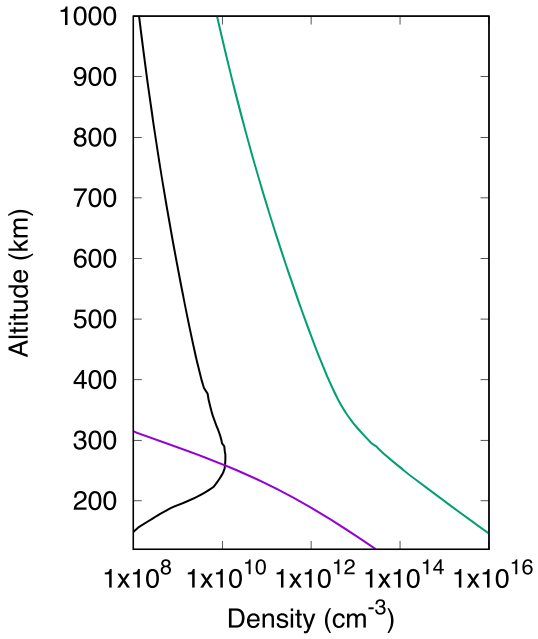

Figure 1. Vertical distribution of the number density of H_2 (green), H (black), and CH_4 (magenta) used in the ionospheric model.

This intensity is scaled up by a factor of 8.1 to get the total H_2 Lyman and Werner bands UV brightness. It is then converted into a precipitating energy flux F_e using the approximation that 10 kR of H_2 emission correspond to an electron precipitation of 1 mW/m^2 (Gérard & Singh, 1982; Grodent et al., 2001; Gustin et al., 2016). The H_2 emissions below ~140 nm can be partly absorbed by methane if they take place near or below the homopause (~1 μbar). In these conditions, the ratio of two spectral bands R = I(155–162 nm)/I(123–130 nm) can be used as a proxy of the electron penetration depth into the atmosphere and therefore of the average energy of precipitating particles. The relation between the ultraviolet color and the initial electron energy is taken from Gérard et al. (2002) and Gustin et al. (2006, 2016) calculated using the neutral model A described by Grodent et al. (2001) for all locations. In this study, we determine the 126–130 nm brightness instead of the classical 123–130 nm range to avoid contamination by the UVS line spread function longward of Lyman-α. We accounted for this slight change of the color ratio definition to convert the color ratio into electron energy flux.

The determination of the local energy flux and mean electron energy quantities allows creating ionospheric conductance maps. The two-parameter description of precipitating electrons (F_e, E_0) is fed into an ionosphere model describing the generation and loss of the different ion species (see supporting information). The vertical distributions of H_3^+, heavy ions, and electrons are then calculated for each UVS pixel. The Pedersen conductivity is integrated with respect to altitude to determine the two-dimensional distribution of the Pedersen conductance.

3. Conductivity and Conductance

We now describe the model used to calculate the contribution of the ions that mostly control the altitude distribution of the Pedersen conductivity. We then describe the dependence of the altitude-integrated conductivity (conductance) versus the electron energy flux and the mean electron energy and the result of some sensitivity tests.

3.1. Ionospheric Model Description

We have developed a simplified ionospheric model to calculate the steady state auroral ionospheric conductivity corresponding to each UVS image pixel. The input quantities are the atmospheric densities of H_2, H, and CH_4, temperature, the energy flux of the precipitation electrons F_e, their characteristic energy E_0, and the local magnetic field. We adopt the H_2, H, and CH_4 number density profiles displayed in Figure 1. It was calculated by Grodent et al.'s (2001) one-dimensional model. This neutral atmosphere model has been widely used in Jovian auroral studies as it is rooted in satellite observations.

The volume ionization rate q(z) is calculated for a given set of E_0 and F_e values, using the analytic expressions given by Hiraki and Tao (2008). They showed that this formulation provides a very good approximation to Monte Carlo calculations. We assume a mean energy loss ΔE of 30 eV to create an ion pair in H_2. The H_2^+ ions quickly transfer their charge via the reaction:

$$H_2^+ + H_2 \rightarrow H_3^+ + H$$

so that the H_3^+ production is in good approximation equal to the H_2^+ production rate. The H_3^+ density at photochemical equilibrium is given by $[H_3^+]_z = \{q(z)/\alpha)\}^{0.5}$, where α is the H_3^+ recombination coefficient. We adopt the value $\alpha = 1.2 \times 10^{-7}(300/T_e)^{0.65}$ cm^3 s^{-1} from Sundström et al. (1994). We adopt the calculated H^+ vertical distribution based on the study by Millward et al. (2002) and linearly scale it with the incident electron energy flux. Sensitivity tests have indicated that the total Pedersen conductance shows negligible dependence on the adopted H^+ ion density over a wide range of scaling factors. Close to and

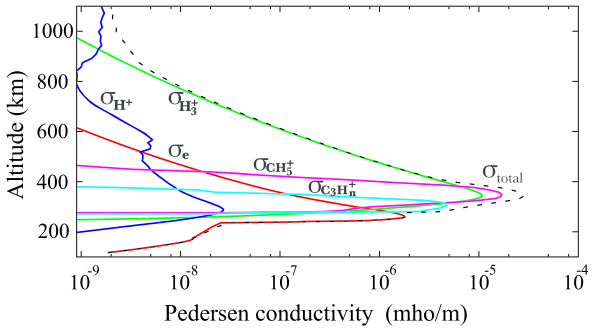

Figure 2. Altitude variation above the 1-bar level of the contributions to the Pedersen conductivity in the auroral ionosphere for a precipitation of 100 mW/m^2 carried by 100 keV electrons. The green curve represents the contribution by H_3^+ ions, purple by CH_5^+, light blue by $C_3H_n^+$, the dark blue by H^+, and red by electrons. The total conductivity is shown by the black dashed line and the conductance is 2.2 mhos.

below the homopause, H_3^+ is rapidly destroyed by reactions with methane and initiates a chain of charge transfer reactions giving rise to a series of hydrocarbon ions. We assume that the electric charge is ultimately transferred to CH_5^+ and $C_3H_n^+$ ions at low altitudes (Perry et al., 1999; Singhal, 1996). To avoid the complexity of solving the neutral-ion chemical coupling, we partition between H_3^+, CH_5^+, and $C_3H_n^+$ according to the fractional ion composition in the aurora calculated by Perry et al. (1999). He estimated that these ions recombine with electrons with total recombination coefficients equal to $2.7 \times 10^{-7}(300/T_e)^{0.52}$ cm^3 s^{-1} and $7.5 \times 10^{-7}(300/T_e)^{0.5}$ cm^3 s^{-1}, respectively, for the sum of the individual reaction channels. The electron density N_e is obtained as the sum of the H_3^+, H^+, and the hydrocarbon ion densities.

Solar EUV radiation generates background Pedersen conductance that varies with local time, especially between day and night. Local maximum values of the conductance produced by solar EUV radiation were estimated to reach 0.0035 mho in the predawn sector and 0.11 mho on the dayside (Tao et al., 2010). It has not been added to the auroral contribution in the maps presented here.

3.2. Conductivity and Conductance

The contribution of ions i with mass m_i to the Pedersen conductivity may be written

$$\sigma^i{}_p = (en_i/B)\ (\nu_{in}\ \omega_i)/\left(\nu_i^2 + \omega_i^2\right) \quad (1)$$

where e the electron charge, n_i is the density of ions i, ν_{in} is the ion-neutral collision frequency (Banks & Kockarts, 1973), ω_i the ion gyration frequency, e the electron charge, and B the magnetic field. The total contribution of the ions is the sum of the contributions of individual ions. Similarly, the electron-neutral conductivity is given by

$$\sigma^e{}_p = (eN_e/B)\ (\nu_{en}\ \omega_e)/\left(\nu_{en}^2 + \omega_e^2\right) \quad (2)$$

with m_e the electron mass, ν_{en} the electron-neutral collision frequency, and ω_e the electron gyration frequency.

The total local conductivity is then given by

$$\sigma^{tot}{}_P = \sigma^e{}_p + \Sigma_i\ \sigma^j{}_{p,} \quad (3)$$

as the sum of the electron and individual ion contributions. The Pedersen conductance Σ_p is the vertically integrated conductivity, expressed in mho.

In a first step, we calculate the vertical distribution of the conductivity for a set of (F_e, E_0) values. Figure 2 shows an example of the total conductivity and contributions given by (1)–(3) for the case F_e = 100 mW m^{-2} and E_0 = 100 keV. In this case, the main contributions are provided by the ions with the exception of the limited region below 300 km where the electron conductivity becomes dominant. The main contributions are provided by collisions of H_3^+ and hydrocarbon ions CH_5^+ and $C_3H_n^+$ ions with the ambient neutral H_2 molecules. As expected, the contribution of H^+ is small in the conductivity region, essentially because of the rarity of H^+ ions relative to the molecular ions. Our tests have confirmed that molecular ion conductivity dominates over electron and H^+ conductivity in the Pedersen conductance for a wide range of energies and electron flux. Since the Pedersen conductance is dominated by the ion-neutral collision term, it can be well approximated by expression (2). It reaches a peak at the altitude where the ion gyrofrequency equals the ion-neutral collision frequency.

More directly relevant to this study, we now describe the variation of conductance (the integrated conductivity) with the initial energy E_0 and the incident electron energy flux F_e at the top of the Jovian atmosphere. For this purpose, the electron transport code coupled to the ionospheric model has been run successive for

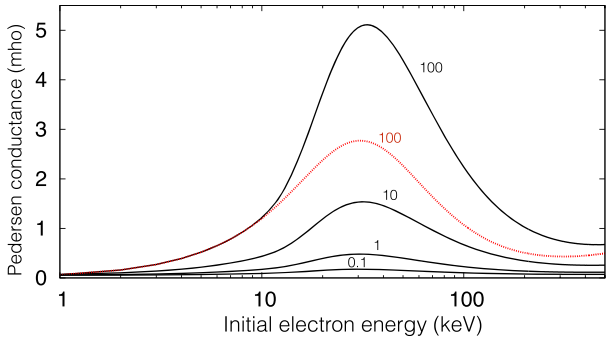

Figure 3. Calculated dependence versus the initial electron energy of the Pedersen conductance for incident electron energy flux (black curves) of 0.1, 1, 10 and 100 mW m^{-2} and a magnetic field intensity of 10 nT. The red curve corresponds to a flux of 100 mW m^{-2} in the case when the charge carried by H_3^+ ions disappears in the reaction with methane near and below the homopause (see text).

F_e = 0.1, 1, 10, and 100 mW/m^2 and E_0 values ranging from 1 to 500 keV by steps of 1 keV. The results are presented in Figure 3 as solid black lines, for a magnetic field of 10 nT, a typical intensity intermediate between highest and lowest values measured in the northern auroral region (Connerney et al., 2018). All curves show a similar shape with a maximum value reached 30 keV. The maximum conductance increases nonlinearly with the energy flux. Indeed, if the mean electron energy is high enough to mostly create H_3^+ ions along their path, both the electron density and the conductivity near the conductivity peak are proportional to the square root of the ionization rate. A similar dependence was predicted by Millward et al. (2002) and Ray et al. (2010) who presented conductance curves exhibiting maximum conductance values for E_0 = 60 keV and 80 keV, respectively, for an incident electron energy flux number of 10 mW m^{-2}. In these conditions, Millward et al. (2002) calculated a peak value of 1.7 mho while Ray et al. (2012) obtained 0.8 mho, compared with 1.5 mho at 32 keV in Figure 3. The decrease of the conductivity beyond 32 keV is related to the increasing depth of the ionization peak that creates H_3^+ ions inside the methane layer where they charge transfer to hydrocarbon ions. CH_5^+ and $C_3H_n^+$ recombine 2.4 and 6.5 times faster with thermal electrons, respectively, than H_3^+. Consequently, the ion density and Pedersen conductivity decreases when the altitude of the peak of ionization decreases.

We have made several simulations to test the sensitivity of the conductance to various parameters. For example, modifications of the magnetic field intensity have shown that Σ_p decreases nonlinearly with increasing B intensity. This is the result of the inverse proportionality on B in the first terms of (2) and (3) combined with the B dependence of the gyrofrequency terms. In another test, the term given by (3) in (4) was set to zero, leading to the conclusion that the electron contribution to the conductance was less than 1%.

Similarly, the importance of H^+ was also found to be negligible in the ion Pedersen conductance relative to that of the H_3^+ and heavier hydrocarbon ions. This is explained by the fact that at low altitudes, H_3^+ and hydrocarbon ions largely dominate by the ion composition and the contribution to the ion conductivity. At high altitude where protons become dominant, the ν/ω ratio steadily decreases and the second term in expression (2) makes negligible contribution to the conductance. A test was conducted to assess the importance of the charge transfer from H_3^+ to heavier ions. The earlier approach (Millward et al., 2002) assumed that following the reaction of H_3^+ ions with methane, the corresponding charge is lost, leading to no contribution to the Pedersen conductance. In our model, the H_3^+ charge is ultimately transferred to CH_5^+ and C_3H_n+ ions. Although these ions have a recombination coefficient and collision frequency different from H_3^+, they still significantly contribute to the conductivity at low altitude when the electron beam penetrates into the methane layer. The importance of this contribution is illustrated by the red curve in Figure 3 showing a simulation where the H_3^+ charge is lost whenever this ion reacts with CH_4. In this case, the maximum

Table 1
Characteristic of Reconstructed FUV Spectral Images in Figures 4 and 5

PJ-(S/N)	Date	Start time	Stop time	S_{III} longitude of the Sun	Juno altitude (R_J)
PJ1-N	27 Aug. 2016	10:07:42	10:58:21	85°–116°	3.48–2.41
PJ3-N	11 Dec. 2016	15:32:22	16:22:43	30°–61°	1.94–0.76
PJ6-S	19 May 2017	06:28:50	07:18:48	225°–255°	0.44–1.64
PJ8-N	01 Sep. 2017	20:06:02	20:56:18	317°–348°	2.20–1.03
PJ10-S	16 Dec. 2017	18:34:49	19:25:55	11°–42°	0.67–1.90
PJ12-N	01 Apr 2018	07:56:41	08:47:50	94°–125°	2.34–1.16
PJ12-S	01 Apr 2018	10:50:26	11:41:33	199°–230°	1.32–2.50
PJ15-S	07 Sep 2018	01:42:24	02:31:55	31°–61°	0.49–1.69

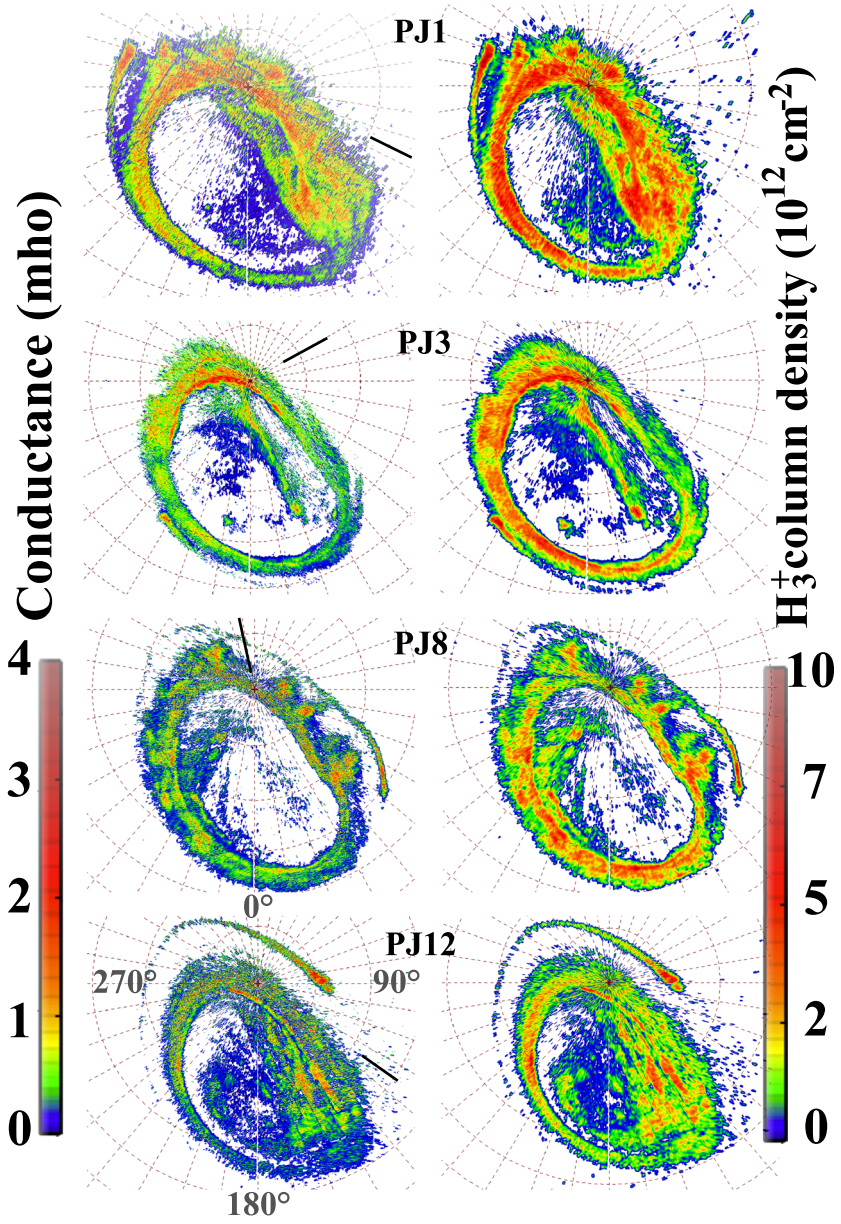

Figure 4. Polar projection of the conductance (left) and H_3^+ column (right) calculated for Junon perijoves 1, 3, 8, and 12 in the north. The 0° System III meridian is oriented upward and longitudes increase clockwise. The short black lines on the conductance maps indicate the mean direction of the Sun during the observations. Projections of the H_2 brightness and color ratio are shown in Figures S1 to S4 in the supporting information.

value of Σ_p drops from 5.1 mhos at 33 keV to 2.7 mhos and by a larger factor at higher energies. We also note that the asymmetry of the red curve is more pronounced than the black curve since; in this case, the H_3^+ ions are lost at low altitudes.

4. Application to the UVS Images of the Jovian Aurora

Maps of the auroral conductance have been constructed on the basis of spectral imaging observations of Jupiter's aurora with UVS. We have selected four Juno orbital segments and the North and four in the South to construct maps of the Pedersen conductance corresponding to these time periods. A time interval on the order of 50 min, best compromise between the spatial coverage and resolution has been determined

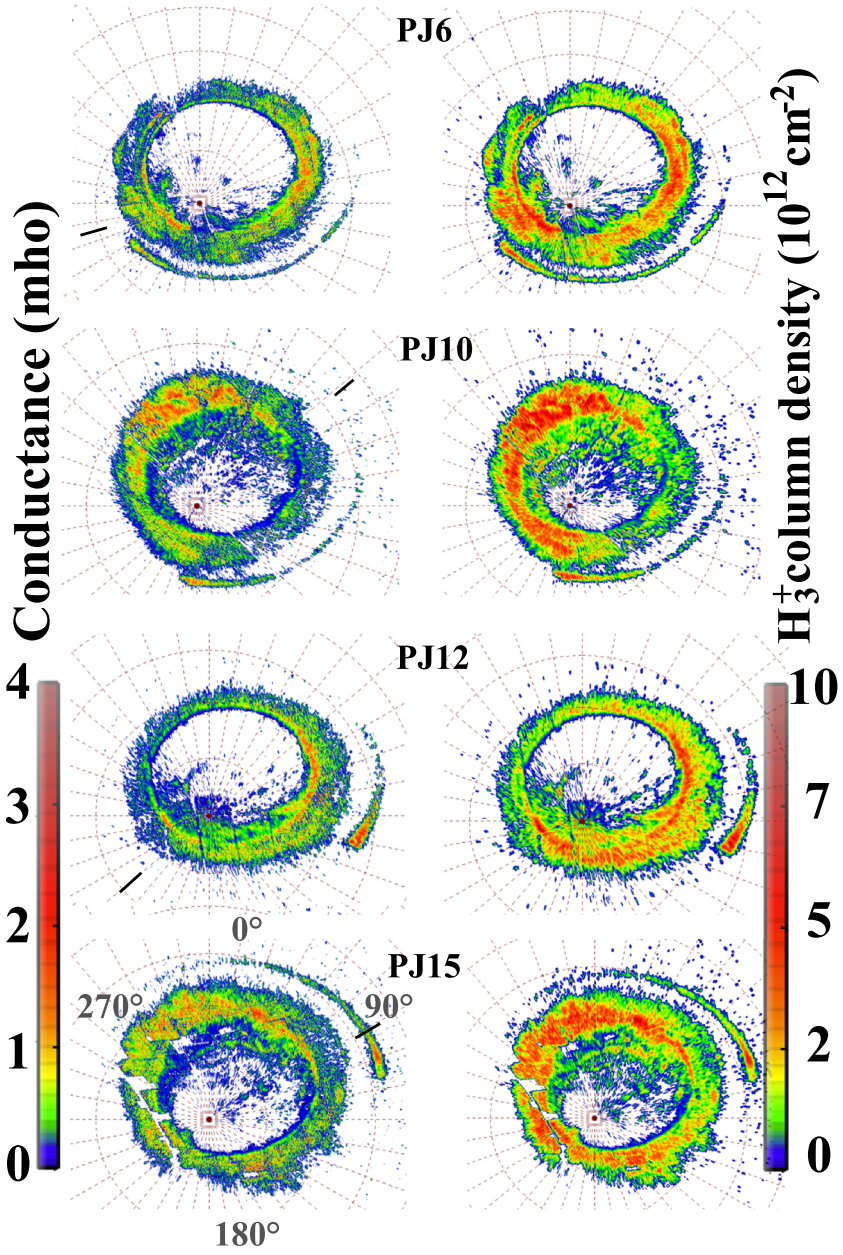

Figure 5. Polar projection of the conductance (left) and H_3^+ column (right) calculated for Juno perijoves 6, 10, 12, and 15 in the south. The 0° System III meridian is oriented upward and longitudes increase clockwise as if the aurora was seen through the planet. The short black lines on the conductance maps indicate the mean direction of the Sun during the observations. Projections of the H_2 brightness and color ratio are shown in panels (a) of Figures S1 to S4 in the supporting information. Projections of the H_2 brightness and color ratio are shown in Figures S5 to S8 in the supporting information.

for each orbit. The dates and times of each of them are listed in Table 1. They have been selected to illustrate a variety of conditions: the two hemispheres, different levels of auroral brightness and color ratio, filling of the polar region and orientation relative to the Sun direction. H_3^+ column density maps are also generated for comparison with values deduced from infrared observations. Figures 4 and 5 show the conductance and H_3^+ column density maps in the north and south, respectively. The conductance maps show a large spatial variability with values ranging from less than 0.1 to more than 5 mhos. All values remain less than 10 mhos. The highest Σ_p values are associated with bright auroral regions such as sections of the main emission, high-latitude diffuse aurora, and the Io auroral spot. Their spatial structure closely resembles that of the

H_3^+ column density, as expected from the dominance of the H_3^+ contribution in the Pedersen conductivity formula. They reach similar values in bright regions of the two hemispheres. Relatively large conductances are associated with the Io spots, as evidences for PJ12-north, where the Σ_p in the Io auroral footprint exceeds the conductivity of any other component of the aurora. These large values are a consequence of the large brightness (and energy flux) associated with the spots and their moderate color ratio.

Figures 4 and 5 also illustrate the calculated spatial distribution of the column of H_3^+ ions, taking into account the loss of these ions following reaction with methane. As for the conductance, the H_3^+ column density is quite variable both spatially and between different orbits, ranging from a few 10^{11} cm^{-2} to about 5×10^{12} cm^{-2}. Similarly to the conductance, PJ1-north shows more extended areas of large column densities than the other cases illustrated here. In the south, the conductance and H_3^+ column reach similar levels to those in the north. An example of measurements made about 3 hr apart in the two hemispheres is illustrated with orbit PJ12.

Brightness, color ratio, H_3^+ column density and conductance maps for the eight perijoves are provided in the supplementary information files S1 to S8.

5. Discussion

As clearly visible in Figures 4 and 5, the H_3^+ column density varies spatially in the aurora by more than an order of magnitude and shows a morphology similar to the calculated Pedersen conductance. The largest values are generally associated with the bright auroral regions. This is an important factor when comparing with values used in earlier models of the Jovian M-I coupling. It is important to stress that the conductance derived in this study is not the effective one accounting for the slippage of the neutral atmosphere from rigid corotation as introduced by Nichols and Cowley (2004), but the original one defined by expressions (1) to (3).

The H_3^+ columns shown in Figures 4 and 5 may be compared with those derived from ground-based infrared spectra of the auroral regions. They were found to range from less than 1×10^{11} to more than 1.5×10^{12} cm^{-2} in regions of bright emission by Lam et al. (1997), although ambiguity remained between the temperature and H_3^+ column determinations. Stallard et al. (2002) also found columns in excess of 1×10^{12} cm^{-2} associated with intensity peaks in spatially resolved cuts across the aurora. Raynaud et al. (2004) mapped column densities generally less than 1×10^{12} cm^{-2}. Moore et al.'s (2017) ground-based auroral maps show H_3^+ columns as large as 1×10^{13} cm^{-2} on and poleward of the statistical location of the main emission. Interestingly, Dinelli et al. (2017) analyzed observations made in the north with the Jovian InfraRed Auroral Mapper (JIRAM) on board Juno during the first Juno orbit. They found H_3^+ columns in excess of 2.8×10^{12} cm^{-2} associated with the bright main emission observed during PJ1-north. This value may be compared with the column map shown in Figure 4 for the same orbit. Our H_3^+ maps show columns up to 5×10^{12} cm^{-2} in regions of strong electron precipitation. The agreement with those derived from spectroscopic investigations may be considered as satisfactory given the limited spatial resolution of the JIRAM H_3^+ map compared with the UVS data and the time delay separating the FUV and the JIRAM images. The differences between earlier conductance models are mostly explained by the different assumptions leading to a variety of different electron energy fluxes and mean electron energy.

A series of tests were also made to assess the sensitivity to various assumptions and limitations.

- First, we vary the intensity of the magnetic field. We find that the Pedersen conductance decreases nonlinearly with increasing B-field magnitude. This and other simulations confirm the importance of using an appropriate B-field model such as JRM09 to estimate the local conductivity (Connerney et al., 2018).
- As shown by Figure 1 and simulations for several different auroral conditions, the Pedersen conductance is essentially controlled by the H_3^+ density distribution, with negligible contribution from electrons and H^+.
- Another source of discrepancy with earlier models stems from the fate of the electric charge carried by H_3^+ ions after they react with methane near and below the homopause. Earlier studies did not include consideration of the carbonated ions as charge carriers. To test the importance of these ions, we assume that the electric charges carried by H_3^+ ions are lost following reaction with methane. The result is illustrated by the red curve in Figure 2. In this case, the conductance drops by about 40% at 30 keV and by an even larger factor at higher electron energies. We also note that the value of the methane density is

less important if the electric charge of H_3^+ ions is transferred to heavier ions at low altitude than if it is lost following their reaction with CH_4.

- A key quantity in converting UV spectral maps to conductance is the relationship between the FUV color ratio and the mean electron energy. It depends on the vertical methane density distribution that has never been directly measured at high latitudes. The relation adopted here (from Grodent et al.'s (2001) model atmosphere) has been abundantly used in the literature. However, the methane density may be locally enhanced by the precipitation and spatially redistributed in the auroral region in a complex way involving a number of poorly constrained quantities.
- The electron energy spectra and pitch angle distributions measured by the Jupiter Energetic Particle Detector Instrument (JEDI) on board Juno in the auroral region show a variety of shapes and intensity. Only rarely is the spectrum at Juno's altitude a peaked distribution at high energy. Instead, the electron flux distribution is usually a broadband spectrum showing a plateau below some variable characteristic energy, followed by a quasi-power law distribution (Clark et al., 2018). In this study, we only consider the case of monoenergetic precipitation whose energy is related in a complex way to the actual energy distribution reaching the atmosphere.

6. Summary and Conclusions

The enhanced Pedersen conductance Σ_p in the Jovian aurora exerts direct control on the currents flowing between the magnetosphere and the ionosphere by increasing the efficiency of the transfer of the planet's angular momentum to the plasma of the magnetosphere. In this study, we used the characteristics of the electron precipitation derived from the UVS spectral images. The electron energy flux and their characteristic energy are used to calculate the vertical distribution of the Pedersen conductivity for each pixel of UVS images. For this purpose, we calculate the vertical distribution of H_3^+ and hydrocarbon ions and evaluate the altitude dependent Pedersen conductivity. We find that

- the only important contribution to this conductance is the term describing the collisions of H_3^+ and hydrocarbon ions with the neutrals;
- for a given electron energy flux, the conductance is maximum for electrons with initial energy ~30 keV;
- hydrocarbon ions contribute as much as 50% to Σ_p when the auroral electrons penetrate below the homopause;
- the auroral conductance is spatially very variable with largest values reached in the regions of the main emission, bright polar patches, and Io's magnetic footprint;
- it is also variable in time and quite inhomogeneous in space, even inside the main region of precipitation;
- the auroral conductance does not locally exceed ~5 mhos, although we expect it can be even larger during periods of dawn storms;
- it may be as small as 0.1 mho or less, similar to the background value at middle and low sunlit latitudes; and
- values are on the same order of magnitude between the north and south auroral regions.

Further analysis based on a larger sample of UVS images will analyze whether an asymmetry of the Pedersen conductance is observed between the two hemispheres. This possibility was raised by Kotsiaros et al. (2019) who found that the Pedersen current density in the south is generally larger than in the north aurora. Similarly, the effect of a distributed electron energy spectrum rather than a monoenergetic precipitation will be discussed in a future study.

Acknowledgments

J.C.G., D.G., Z.Y., and A.R. acknowledge financial support from the Belgian Federal Science Policy Office via the ESA's PRODEX. B.B. is a Research Associate of the Fonds National de la Recherche Scientifique —FNRS. We are grateful to NASA and contributing institutions that have made the Juno mission possible. The UltraViolet Imager/Spectrograph work was funded by NASA's New Frontiers Program for Juno via a subcontract with the Southwest Research Institute. Juno operations are supported by NASA (managed by the Jet Propulsion Laboratory). Michel Blanc acknowledges the support of CNES to his involvement in NASA's JUNO mission, and the support of CNRS and University Toulouse III – Paul Sabatier.

Data Availability Statement

The Juno UVS data used for this study are archived and available in NASA's Planetary Data System (https://pds-atmospheres.nmsu.edu/data_and_services/atmospheres_data/JUNO/uvs.html).

References

Achilleos, N., Miller, S., Tennyson, J., Aylward, A. D., Mueller-Wodarg, I., & Rees, D. (1998). JIM: A time-dependent, three-dimensional model of Jupiter's thermosphere and ionosphere. *Journal of Geophysical Research*, *103*(E9), 20089–20112. https://doi.org/10.1029/98JE00947

Badman, S. V., Branduardi-Raymont, G., Galand, M., Hess, S. L. G., Krupp, N., Lamy, L., et al. (2015). Auroral processes at the giant planets: Energy deposition, emission mechanisms, morphology and spectra. *Space Science Reviews*, *187*(1-4), 99–179. https://doi.org/10.1007/s11214-014-0042-x

Bagenal, F., Adriani, A., Allegrini, F., Bolton, S. J., Bonfond, B., Bunce, E. J., et al. (2017). Magnetospheric science objectives of the Juno mission. *Space Science Reviews*, *213*(1–4), 219–287. https://doi.org/10.1007/s11214-014-0036-8

Banks, P. M., & Kockarts, G. (1973). *Aeronomy*. New-York: Academic Press.

Bolton, S. J., Lunine, J., Stevenson, D., Connerney, J. E. P., Levin, S., Owen, T. C., et al. (2017). The Juno mission. *Space Science Reviews*, *213*(1–4), 5–37. https://doi.org/10.1007/s11214-017-0429-6

Bonfond, B., Gladstone, G. R., Grodent, D., Greathouse, T. K., Versteeg, M. H., Hue, V., et al. (2017). Morphology of the UV aurorae Jupiter during Juno's first perijove observations. *Geophysical Research Letters*, *44*, 4463–4471. https://doi.org/10.1002/2017GL073114

Bougher, S. W., Waite, J. H. Jr., Majeed, T., & Gladstone, G. R. (2005). Jupiter Thermospheric General Circulation Model (JTGCM): Global structure and dynamics driven by auroral and Joule heating. *Journal of Geophysical Research*, *110*, E04008. https://doi.org/10.1029/2003JE002230

Clark, G., Tao, C., Mauk, B. H., Nichols, J., Saur, J., Bunce, E. J., et al. (2018). Precipitating electron energy flux and characteristic energies in Jupiter's main auroral region as measured by Juno/JEDI. *Journal of Geophysical Research: Space Physics*, *123*, 7554–7567. https://doi.org/10.1029/2018JA025639

Clarke, J. T., Grodent, D., Cowley, S. W., Bunce, E. J., Zarka, P., Connerney, J. E., & Satoh, T. (2004). Jupiter's aurora. *Jupiter: The Planet, Satellites and Magnetosphere*, *1*, 639–670.

Connerney, J. E. P., Kotsiaros, S., Oliversen, R. J., Espley, J. R., Joergensen, J. L., Joergensen, P. S., et al. (2018). A new model of Jupiter's magnetic field from Juno's first nine orbits. *Geophysical Research Letters*, *45*, 2590–2596. https://doi.org/10.1002/2018GL077312

Coumans, V., Gérard, J. C., Hubert, B., Meurant, M., & Mende, S. B. (2004). Global auroral conductance distribution due to electron and proton precipitation from IMAGE-FUV observations. *Annales Geophysicae*, *22*(5), 1595–1611. https://doi.org/10.5194/angeo-22-1595-2004

Cowley, S. W. H., & Bunce, E. J. (2001). Origin of the main auroral oval in Jupiter's coupled magnetosphere–ionosphere system. *Planetary and Space Science*, *49*(10-11), 1067–1088. https://doi.org/10.1016/S0032-0633(00)00167-7

Dinelli, B. M., Fabiano, F., Adriani, A., Altieri, F., Moriconi, M. L., Mura, A., et al. (2017). Preliminary JIRAM results from Juno polar observations: 1. Methodology and analysis applied to the Jovian northern polar region. *Geophysical Research Letters*, *44*, 4625–4632. https://doi.org/10.1002/2017GL072929

Gérard, J. C., Bonfond, B., Mauk, B. H., Gladstone, G. R., Yao, Z. H., Greathouse, T. K., et al. (2019). Contemporaneous observations of Jovian energetic auroral electrons and ultraviolet emissions by the Juno spacecraft. *Journal of Geophysical Research: Space Physics*, *124*, 8298–8317. https://doi.org/10.1029/2019ja026862

Gérard, J. C., Gustin, J., Grodent, D., Delamere, P., & Clarke, J. T. (2002). The excitation of the FUV Io tail on Jupiter: Characterization of the electron precipitation. *Journal of Geophysical Research*, *107*(A11), 1394. https://doi.org/10.1029/2002JA009410

Gérard, J. C., & Singh, V. A. (1982). Model of energetic electrons and EUV emission in the Jovian and Saturnian atmospheres and implications. *Journal of Geophysical Research*, *87*, 4525.

Germany, G. A., Torr, D. G., Richards, P. G., Torr, M. R., & John, S. (1994). Determination of ionospheric conductivities from FUV auroral emissions. *Journal of Geophysical Research*, *99*(A12), 23297–23,305. https://doi.org/10.1029/94JA02038

Gladstone, G. R., Persyn, S. C., Eterno, J. S., Walther, B. C., Slater, D. C., Davis, M. W., et al. (2017). The ultraviolet spectrograph on NASA's Juno mission. *Space Science Reviews*, *213*(1–4), 447–473. https://doi.org/10.1007/s11214-014-0040-z

Grodent, D., Waite, J. H. Jr., & Gérard, J. C. (2001). A self-consistent model of the Jovian auroral thermal structure. *Journal of Geophysical Research*, *106*(A7), 12933–12952. https://doi.org/10.1029/2000JA900129

Gustin, J., Cowley, S. W. H., Gérard, J.-C., Gladstone, G. R., Grodent, D., & Clarke, J. T. (2006). Characteristics of Jovian morning bright FUV aurora from Hubble space telescope/space telescope imaging spectrograph imaging and spectral observations. *Journal of Geophysical Research*, *111*, A09220. https://doi.org/10.1029/2006JA011730

Gustin, J., Grodent, D., Ray, L. C., Bonfond, B., Bunce, E. J., Nichols, J. D., & Ozak, N. (2016). Characteristics of north Jovian aurora from STIS FUV spectral images. *Icarus*, *268*, 215–241. https://doi.org/10.1016/j.icarus.2015.12.048

Hiraki, Y., & Tao, C. (2008). Parameterization of ionization rate by auroral electron precipitation in Jupiter. *Annales de Geophysique*, *26*(1), 77–86. https://doi.org/10.5194/angeo-26-77-2008

Kotsiaros, S., Connerney, J. E. P., Clark, G., Allegrini, F., Gladstone, G. R., Kurth, W. S., et al. (2019). Birkeland currents in Jupiter's magnetosphere observed by the polar-orbiting Juno spacecraft. *Nature Astronomy*, *3*(10), 904–909. https://doi.org/10.1038/s41550-019-0819-7

Lam, H. A., Achilleos, N., Miller, S., Tennyson, J., Trafton, L. M., Geballe, T. R., & Ballester, G. E. (1997). A baseline spectroscopic study of the infrared auroras of Jupiter. *Icarus*, *127*(2), 379–393. https://doi.org/10.1006/icar.1997.5698

Majeed, T., Waite, J. H., Bougher, S. W., & Gladstone, G. R. (2009). Processes of auroral thermal structure at Jupiter: Analysis of multi-spectral temperature observations with the JTGCM. *Journal of Geophysical Research*, *114*, E07005. https://doi.org/10.1029/2008JE003194https://wiley.eproofing.in/Proof.aspx?token=32c88f3ec2f543c1ae52b79b0e73736e015928996#com3

Millward, G., Miller, S., Stallard, T., Aylward, A. D., & Achilleos, N. (2002). On the dynamics of the Jovian ionosphere and thermosphere: III The modelling of auroral conductivity. *Icarus*, *160*(1), 95–107. https://doi.org/10.1006/icar.2002.6951

Moore, L., O'Donoghue, J., Melin, H., Stallard, T., Tao, C., Zieger, B., et al. (2017). Variability of Jupiter's IR H_3^+ aurorae during Juno approach. *Geophysical Research Letters*, *44*, 4513–4522. https://doi.org/10.1002/2017GL073156

Nichols, J. D., & Cowley, S. W. H. (2004). Magnetosphere-ionosphere coupling currents in Jupiter's middle magnetosphere: Effect of precipitation-induced enhancement of the ionospheric Pedersen conductivity. *Annales Geophysicae*, *22*(5), 1799–1827. https://doi.org/10.5194/angeo-22-1799-2004

Perry, J. J., Kim, Y. H., Fox, J. L., & Porter, H. S. (1999). Chemistry of the Jovian auroral ionosphere. *Journal of Geophysical Research*, *104*(E7), 16541–16565. https://doi.org/10.1029/1999JE900022

Ray, L. C., Achilleos, N. A., & Yates, J. N. (2015). The effect of including field-aligned potentials in the coupling between Jupiter's thermosphere, ionosphere, and magnetosphere. *Journal of Geophysical Research: Space Physics*, *120*, 6987–7005. https://doi.org/10.1002/2015JA021319

Ray, L. C., Ergun, R. E., Delamere, P. A., & Bagenal, F. (2010). Magnetosphere-ionosphere coupling at Jupiter: Effect of field-aligned potentials on angular momentum transport. *Journal of Geophysical Research*, *115*, A09211. https://doi.org/10.1029/2010JA015423

Ray, L. C., Ergun, R. E., Delamere, P. A., & Bagenal, F. (2012). Magnetosphere-ionosphere coupling at Jupiter: A parameter space study. *Journal of Geophysical Research*, *117*, A01205. https://doi.org/10.1029/2011JA016899

Raynaud, E., Lellouch, E., Maillard, J.-P., Gladstone, G. R., Waite, J. H., Bezard, B., et al. (2004). Spectro-imaging observations of Jupiter's 2 μm auroral emission. I. H_3^+ distribution and temperature. *Icarus*, *171*(1), 133–152. https://doi.org/10.1016/j.icarus.2004.04.020

Singhal, R. P. (1996). Hall and Pedersen conductivities in the auroral ionosphere of Jupiter. *Indian Journal of Radio & Space Physics*, 361–366.

Smith, C. G. A., & Aylward, A. D. (2009). *Annales Geophysicae*, *27*, 199–230.

Stallard, T., Miller, S., Millward, G., & Joseph, R. D. (2002). On the dynamics of the Jovian ionosphere and thermosphere. II. The measurement of H_3^+ vibrational temperature, column density, and total emission. *Icarus*, *156*(2), 498–514. https://doi.org/10.1006/icar.2001.6793

Strobel, D. F., & Atreya, S. K. (1983). Ionosphere. In A. Dessler (Ed.), *Physics of the Jovian Magnetosphere* (pp. 51–67). England: Cambridge Univ. Press. https://doi.org/10.1017/CBO9780511564574.004

Sundström, G., Mowat, J. R., Danared, H., Datz, S., Broström, L., Filevich, A., et al. (1994). Destruction rate of H_3^+ by low-energy electrons measured in a storage-ring experiment. *Science*, *263*(5148), 785–787. https://doi.org/10.1126/science.263.5148.785

Tao, C., Fujiwara, H., & Kasaba, K. (2009). Neutral wind control of the Jovian magnetosphere–ionosphere current system. *Journal of Geophysical Research*, *114*, A08307. https://doi.org/10.1029/2008JA013966

Tao, C., Fujiwara, H., & Kasaba, Y. (2010). Jovian magnetosphere-ionosphere current characterized by diurnal variation of ionospheric conductance. *Planet Space Science*, *58*(3), 351–364. https://doi.org/10.1016/j.pss.2009.10.005

References From the Supporting Information

Bonfond, B., Gustin, J., Gérard, J.-C., Grodent, D., Radioti, A., Palmaerts, B., et al. (2015). The far-ultraviolet main auroral emission at Jupiter—Part 2: Vertical emission profile. *Annales Geophysicae*, *33*(10), 1211–1219. https://doi.org/10.5194/angeo-33-1211-2015

Hue, V., Gladstone, G. R., Greathouse, T. K., Kammer, J. A., Davis, M. W., Bonfond, B., et al. (2019). In-flight characterization and calibration of the Juno-Ultraviolet Spectrograph (Juno-UVS). *The Astronomical Journal*, *157*(2), 90. https://doi.org/10.3847/1538-3881/aafb36

Nichols, J. D. (2011). Magnetosphere-ionosphere coupling in Jupiter's middle magnetosphere: Computations including a self-consistent current sheet magnetic field model. *Journal of Geophysical Research*, *116*, A10232. https://doi.org/10.1029/2011JA016922